JGR Solid Earth

RESEARCH ARTICLE
10.1029/2019JB017354

Drought-Triggered Magmatic Inflation, Crustal Strain, and Seismicity Near the Long Valley Caldera, Central Walker Lane

W. C. Hammond[1], C. Kreemer[1], I. Zaliapin[2], and G. Blewitt[1]

[1]Nevada Geodetic Laboratory, Nevada Bureau of Mines and Geology, University of Nevada, Reno, NV, USA, [2]Department of Mathematics and Statistics, University of Nevada, Reno, NV, USA

Key Points:
- Faster Sierra Nevada uplift during the 2011–2016 drought in California coincided with faster magmatic inflation at the Long Valley Caldera
- Faster magmatic inflation changed the rate and distribution of crustal strain in the Central Walker Lane, >60 km from Long Valley
- Seismicity patterns in the Central Walker Lane suggest that long-term crustal strain may be driven in part by Long Valley magmatic inflation

Supporting Information:
- Supporting Information S1
- Table S1

Correspondence to:
W. C. Hammond,
whammond@unr.edu

Citation:
Hammond, W. C., Kreemer, C., Zaliapin, I., & Blewitt, G. (2019). Drought-triggered magmatic inflation, crustal strain, and seismicity near the Long Valley Caldera, Central Walker Lane. *Journal of Geophysical Research: Solid Earth*, *124*. https://doi.org/10.1029/2019JB017354

Received 14 JAN 2019
Accepted 19 MAY 2019
Accepted article online 24 MAY 2019

Abstract We use GPS data to show synchronization between the 2011 and 2016 drought cycle in California, accelerated uplift of the Sierra Nevada Mountains, and enhanced magmatic inflation of the Long Valley Caldera (LVC) magmatic system. The drought period coincided with faster uplift rate, changes in gravity seen in the Gravity Recovery and Climate Experiment (GRACE), and changes in standardized relative climate dryness index. These observations together suggest that the Sierra Nevada elevation is sensitive to changes in hydrological loading conditions, which subsequently influences the LVC magmatic system. We use robust imaging of horizontal GPS velocities to derive time-variable shear and dilatational strain rates in a region with highly variable station distribution. The results show that the highest strain rates are near the eastern margin of the Sierra Nevada and western edge of the Central Walker Lane (CWL) passing directly through LVC. The drought period saw geographic shifts in the distribution in active shear strain in the CWL more than 60 km from the LVC, delineating the minimum extent over which the active magmatic system affects the CWL tectonic environment. We analyze declustered seismicity data to show that locations with higher seismicity rates tend to be (1) areas with higher strain rates and (2) areas in which strain rates increased during drought-enhanced inflation. We hypothesize that drought conditions reduce vertical surface mass loading, which decreases pressure at depth in the LVC system, in turn enhances magmatic inflation, and drives horizontal elastic stress changes that redistribute active CWL strain and modulate seismicity.

Plain Language Summary We show that there were connections between the recent drought in California to changes in uplift rate of the Sierra Nevada, magmatic inflation at the Long Valley Caldera near Mammoth, CA, and earthquakes in the region. We use GPS, seismic, gravity, and climate data to show that the speed of uplift of the Sierra Nevada is sensitive to big changes in surface and groundwater (e.g., in snow, streams, lakes, and aquifers) and that these changes correlate with movements within the large volcano. A plausible explanation is that the weight of snow and water loads the surface and changes pressures deep in the Earth. As the Sierra Nevada was unloaded during recent drought, there was less pressure on the magmatic system, allowing fluids to rise or expand more easily. When that occurred, it provided an outward horizontal push on the crust, influencing small- to moderate-sized earthquakes up to 60 km away. We show where and when these changes occurred and specific examples of earthquakes that may have been triggered by this inflation.

1. Introduction

Recent studies have shown that active uplift of the Sierra Nevada Mountains in California and Nevada, western United States, is detectible in vertical component GPS measurements, with rates up to 2 mm/yr (Fay et al., 2008; Hammond et al., 2012). The geographic pattern and seasonality of the signals provide clear indications that surface mass unloading from loss of ground and surface water help drive the observed uplift (Amos et al., 2014; Argus et al., 2017; Kreemer & Zaliapin, 2018). As California entered severe drought conditions in late 2011, precipitation decreased and was followed by an intensification of the extraction of groundwater and reduction in water availability in California Central Valley aquifers (e.g., Faunt et al., 2016). This period also saw the acceleration of uplift of the Sierra Nevada, and other parts of the western United States, where further reduction in the mass of surface and groundwater drove upward inflections in the GPS-measured uplift (Amos et al., 2014; Argus et al., 2017; Borsa et al., 2014; Hammond et al., 2016).

Immediately east of this region of time-variable uplift and the Sierra Nevada lies a zone of active tectonic shear and extension known as the Walker Lane. Here the magmatically active Long Valley Caldera (LVC) straddles the Sierra Nevada range front fault system (Figure 1). It also lies at a structural transition between the Southern Walker Lane, composed of the Sierra Nevada range front normal fault and north-northwest trending right-lateral faults, and the Northern Walker Lane composed of a system of discontinuous en echelon normal fault-bounded basins (Wesnousky et al., 2012). Between them and east of LVC lie the easterly striking left-lateral faults of the Mina Deflection, which form a right step across the Walker Lane system over which slip is transferred from southern to northern Walker Lane (Wesnousky, 2005). As a whole the Walker Lane accommodates about one fifth of the relative tectonic motion between the Pacific and North American plates (e.g., Bennett et al., 2003; Hammond & Thatcher, 2007; Lifton et al., 2013; Oldow et al., 2001; Thatcher et al., 1999). Embedded within this zone, the LVC experiences periods of volcanic unrest with magmatic inflation, enhanced seismicity, and high uplift rates that can be 8 times that of the adjacent Sierra Nevada (Montgomery-Brown et al., 2015).

Owing to the volcanic hazard posed by the LVC, active deformation has been monitored and studied with seismic, geodetic, geochemical, and gravity instrumentation over the past four decades (for summaries, see, e.g., Hill, 2006). The largest component of deformation has been well described with inflation of a volumetric source that lies in the middle crust (6–10 km) beneath the Resurgent Dome near the center of LVC (Battaglia et al., 1999, 2003; Feng & Newman, 2009; Fialko et al., 2001; Hetland et al., 2012; Ji et al., 2013; Langbein et al., 1995, 2003; Montgomery-Brown et al., 2015; Newman et al., 2006; Savage, 1988; Savage & Clark, 1982). To a lesser extent other sources contribute to surface motions including (1) extension north along the Mono/Inyo crater chain (Feng & Newman, 2009; Marshall et al., 1997), (2) a smaller volumetric source beneath the south moat area near the south edge of LVC (Langbein, 1995; Tiampo et al., 2000), (3) and a source in the middle crust beneath Mammoth Mountain at the southwest corner of LVC (Langbein et al., 1993, 1995). The resulting deformation overlaps spatially with both the CWL steady transtension and Sierra Nevada uplift (Figure 1). Owing to time-variable magmatic strain at the LVC, numerous geodetic studies of seismic hazard omit GPS stations near the caldera as a nuisance in modeling of fault slip rates (e.g., McCaffrey, 2005; Petersen et al., 2014; Zeng & Shen, 2014). However, one recent GPS study observed that the transient strain rate anomaly extends as far north as Bridgeport, CA, ~75 km from the LVC (Bormann et al., 2016). An implication is that the transient magmatic strain may extend across a wide swath of the CWL, and the area over which fault slip rate estimates will be affected is larger than previously assumed.

In this study we use GPS data to show that there was synchronization between the recent California drought cycle, enhanced Sierra Nevada uplift, reenergization of LVC magmatic inflation, and crustal seismicity in the CWL outside of the LVC. We use a robust imaging technique known as GPS Imaging (Blewitt et al., 2016; Hammond et al., 2016) to infer the geographic extent and style of deformation signals associated with enhanced magmatic inflation outside the area of the LVC. We then discuss the relationships between the strain rate and timing of recent earthquakes, showing that the drought-enhanced surface unloading of the Sierra Nevada influenced CWL seismicity. We find that the extent of time-variable crustal deformation extends to at least 60 km from the LVC center, showing that it likely affects the tectonic evolution of a large portion of the CWL.

2. Methods: GPS Imaging of Uplift and Strain Rate

We here examine the crustal uplift and strain rates during the drought period and compare them to the pre-drought period. We use GPS Imaging, a technique that provides robust estimates of GPS position time series trends and spatial interpolation, to visualize time variable three-component velocities and strain rate changes. GPS Imaging is composed of two steps. First, we use the MIDAS algorithm, which applies Theil-Sen statistics to make a nonparametric estimate of time series trends that are insensitive to steps, outliers, or heteroskedasticity in the time series (Blewitt et al., 2016). Second, we apply a robust geographic filtering and interpolation that identifies the part of a spatially variable signal that is locally consistent among multiple stations. This uses Delaunay triangulation of the GPS network and evaluates the weighted median of local data at regular grid points, where each estimate is a function only of the values at neighboring stations. The resulting field is robust and insensitive to outlying data of arbitrary magnitude as long as they are isolated, that is, not corroborated by neighboring data. Therefore, the stability and appearance of the

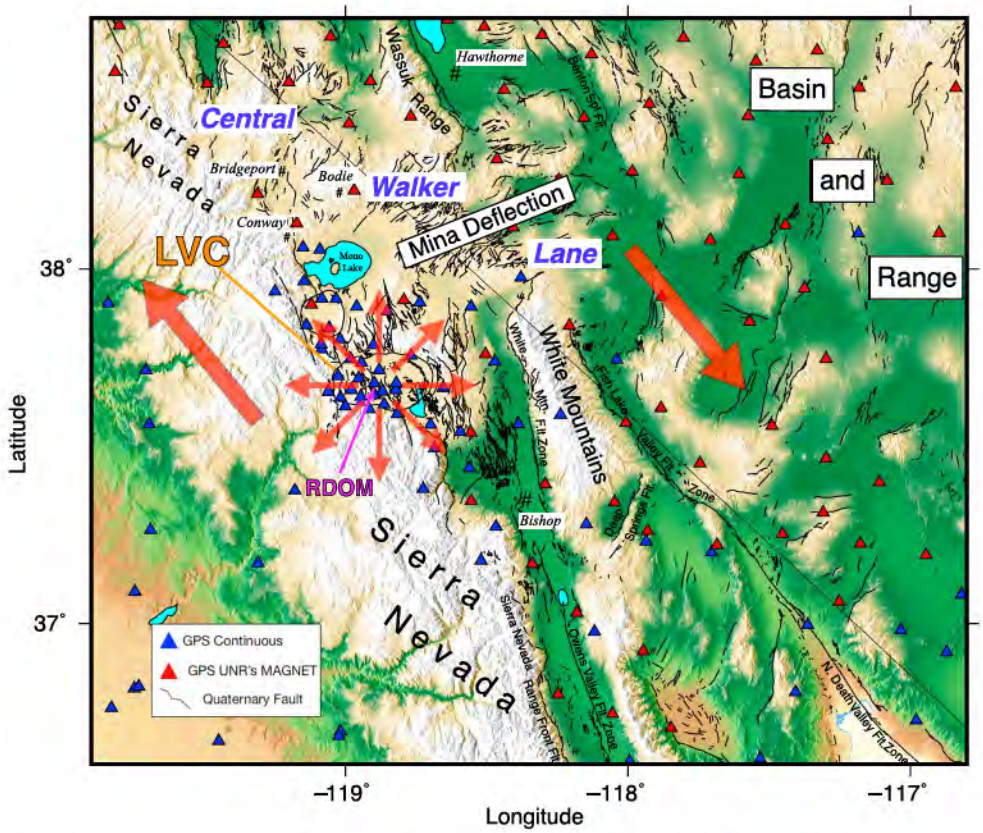

Figure 1. Color-shaded topography of the central Sierra Nevada Mountains, Long Valley Caldera (LVC), and western Great Basin. Triangles are locations of GPS stations from the MAGNET GPS Network (red) and other continuous GPS stations (blue). Black lines are Quaternary faults. Large red arrows indicate general sense of crustal shear across CWL, and smaller red arrows indicate sense of inflation at LVC. Orange text and line segment indicate location of LVC. The location of GPS station RDOM, which sits atop the Resurgent Dome near the center of the LVC, is indicated with the magenta text and arrow. Location of other geographic and tectonic features, such as towns, the Sierra Nevada Mountains, Mina Deflection, Wassuk Range, White Mountains, Basin and Range, and selected active faults are indicated with black text.

inferred field is derived from consensus among the data and not from classical smoothing. The geographic resolution of the imaging is limited only by the station spacing. The method was first used on vertical GPS velocities to image time-variable uplift of the Sierra Nevada (Hammond et al., 2016).

To estimate horizontal strain rates using GPS Imaging, we apply the method to both east and west components of horizontal GPS MIDAS velocities. We use an evenly spaced grid with intervals of 0.05° while the gridded vectors are decimated by a factor of 4 for plotting. We derive strain rates from gradients in the imaged (gridded) horizontal velocity field. We use the relations from Savage et al. (2001) to separate the velocity gradients into components attributable to rigid rotation and internal deformation on a sphere. At each grid point we estimate the local strain rates with a weighted linear inversion, using the gridded velocity values as input data. The weights are a function of distance from the evaluation point, using an exponential that decreases with distance (similar to Shen et al., 1996) of the form

$$w_i = e^{-\left[(|\boldsymbol{x}_i - \boldsymbol{x}_0|/r)^2\right]} \tag{1}$$

$$w_i = w_i / \sum w_i \tag{2}$$

where $|\boldsymbol{x}_i - \boldsymbol{x}_0|$ is the distance between the point where strain rate is being evaluated $\boldsymbol{x}_0$ and the locations of the gridded velocities $\boldsymbol{x}_i$ that are within a distance of 4 times the distance r. The second equation normalizes the weights for each evaluation. Larger values of r result in effectively smoother models with generally

greater misfit to the velocity data. We determined a value of $r = 6$ km through testing of many values in an analysis, which considered the trade-off between model norm and data misfit (supporting information Figure S1). This value is where the model norm begins to decrease less rapidly as r is increased and results in lower model misfit than for higher values of r.

3. Data

3.1. Global Positioning System

We use data from regional high-precision GPS networks summarized in supporting information Table S1. In total, we obtained data from 432 stations that are within 1° outside of the bounds of Figure 1, plus 13 more that appear in Figure 2. All networks collected data continuously except for the MAGNET GPS Network operated by the Nevada Bureau of Mines and Geology at the University of Nevada, Reno. MAGNET data are semicontinuous and thus have observations that are sparser in time (Blewitt et al., 2009). MAGNET data constrain rates of motion nearly as well as continuous stations but in some cases do not well constrain seasonal oscillations since they are only occupied part of each year. Continuous stations are more common on the Sierra Nevada and LVC (since they monitor the active volcanic system), while MAGNET dominates to the east in the Great Basin where time-variable motion was thought to be less prevalent owing to generally drier conditions in the rain shadow of the Sierra Nevada (Amos et al., 2014; Kreemer & Zaliapin, 2018; Figure 1).

We process RINEX data from the GPS stations to estimate daily coordinate time series as part of a global GPS network analysis that includes ~17,000 stations (Blewitt et al., 2018). Our system employs the GIPSY-OASIS II software package in precise positioning mode (Zumberge et al., 1997) to estimate daily station coordinates. We align the daily three-component position solutions with the North America-fixed, spatially filtered reference frame, NA12 (Blewitt et al., 2013). This frame has an origin and scale that are consistent with the International Terrestrial Reference Frame, ITRF2008 (Altamimi et al., 2011) but is fixed to the North American plate and provides a continental-scale regional filtering that reduces common-mode noise in the horizontal and vertical coordinates (Wdowinski et al., 1997). All position solutions and reference frame alignment x-files are posted and available for download on the data products pages of the Nevada Geodetic Laboratory (http://geodesy.unr.edu).

To illustrate the GPS data's consistency and sensitivity and their potential to detect Sierra Nevada steady background uplift, we plot the vertical component of the 19 stations that lie between the Sierra Nevada crest and Central Valley, on the west slope of the Range (Figure 2). We vertically shift each vertical position time series by subtracting the median difference between the data at common epochs and then plot all the time series on the same coordinate axes. The number of stations contributing to the plot increased rapidly in 2006 from about 5 to between 15 and 20, continuing to the present (Figure 2b). The result shows that the trend is generally upward over time between 1996.0, at the beginning of our GPS holdings, and the present. The cumulative gain in median elevation is 24.2 mm, as measured by the median of the last 4 years of data minus the median of the first 4 years of data (red lines in Figure 2) over 23 years. These date ranges are chosen to stack sparse data in the early period and average among drought-affected and nondrought years in the late period. The average background uplift rate for this stack of stations is 1.3 mm/yr, a bit lower than the maximum rates of 1–2 mm/yr found for the southern Sierra Nevada, in part because the uplift rates tend toward zero north of latitude 39° (Argus et al., 2017; Hammond et al., 2012, 2016). The uplift rate for the second half of the time series is ~1.4 mm/yr, which is determined by comparing the later interval to the middle 4 years (2005 to 2009), which is better constrained because of the larger number of stations in the middle interval.

While the trend is persistently upward over the time of observation, it is evident from the time series that the signal is modulated by other time-variable effects that include (1) seasonality in uplift that is similar in amplitude and phase for all the stations and (2) relatively abrupt drops in elevation in 2006, 2011, and 2016 that coincide with years of heavy precipitation in California. While these events occur multiple times during the period of observation, they are not enough to reverse the overall trend of uplift. The seasonal signals are generally wet season-down, dry season-up motions, which are consistent with the Earth's response to changes in hydrological loading. Seasonality in vertical GPS time series has been linked to yearly changes in surface loading from terrestrial water storage (e.g., Amos et al., 2014; Argus et al., 2014; Blewitt et al., 2001; van Dam et al., 2001; Heki, 2000). In the western U.S. intermittent inflections in uplift have been

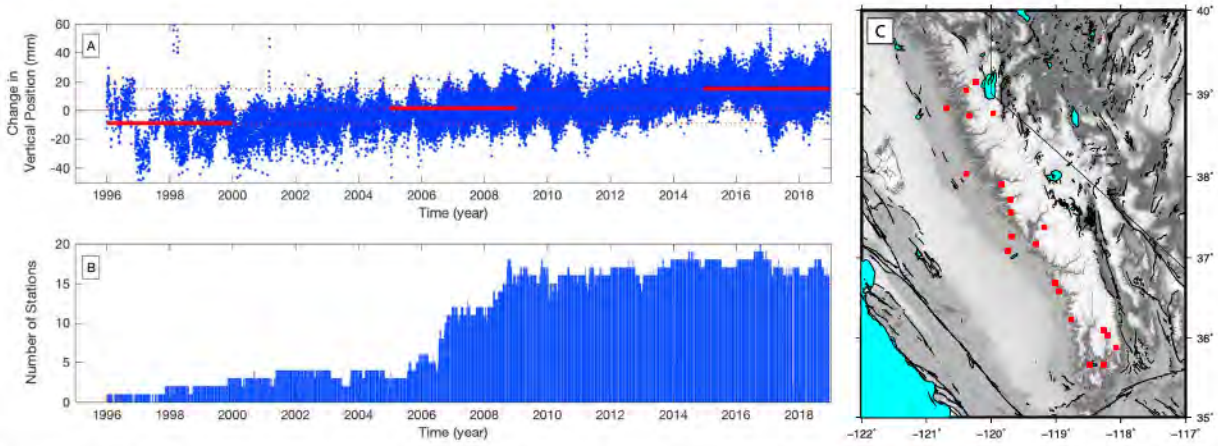

Figure 2. (a) Stack of GPS vertical position time series for stations on the west slope of the Sierra Nevada, shifted to minimize misfit so that the aggregate time series crosses zero near year 2007.0. Red line segments show median relative elevation for early (1996.0–2000.0), middle (2005.0–2009.0), and late (2015–2019) intervals. The difference between the late and early (middle) periods indicates a net increase in elevation of 24.2 (13.7) mm since the earliest (middle) period of GPS observation. The horizontal dotted lines are extensions of the red segments to better visualize the difference between elevations. (b) Number of stations providing data as a function of time. (c) Map showing location of GPS stations (red dots) on Sierra Nevada west slope.

documented to coincide with periods of sustained drought (Argus et al., 2017; Borsa et al., 2014; Hammond et al., 2016), highlighting the sensitivity of the Earth to nonseasonal changes in hydrological loading.

3.2. GRACE

A separate measure of the hydrological loading comes from the Gravity Recovery and Climate Experiment (GRACE) satellites. These data reveal seasonality and trend changes in Earth's gravity field that are caused by changes in surface water mass that drive hydrological loading (Argus et al., 2014, 2017; Famiglietti et al., 2011; Fu et al., 2012; Johnson et al., 2017). We obtained processed GRACE data from MASCON #1895 from the GSFC 1-arc degree solutions (Luthcke et al., 2013) from the University of Colorado, Boulder Mascon viewer (https://ccar.colorado.edu/grace/gsfc.html). These data were available from years 2003.0 to 2016.5 and represent an average water equivalent thickness over an area of 1.2×10^4 km^2 centered approximately over Mono Lake (Figure 1). GRACE data are presented in equivalent water layer thickness needed to create the gravity change, which we plot in a time series in order to compare to the GPS results (Figure 3). The sign of GRACE seasonality is flipped compared to seasonality of uplift, since increasing the effective thickness of the water layer causes increased gravity and lower surface elevation. The same relation holds for the inflections of GRACE data trends compared to the inflections in the GPS uplift data. For example, the downward inflection of the GRACE data that begins in 2011 coincides with the upward inflection in the GPS that begins at the same time. These data help confirm the origin of the seasonality and trend changes in the vertical GPS time series. Also, the fact that there is an overall trend in the GRACE time series suggests the possibility that a longer-term trend in hydrological loading between 2003.0 and 2016.5 is controlling the decadal trend of Sierra Nevada uplift over that period.

3.3. Palmer Drought Severity Index

While the GRACE and GPS data can be used to show the relationship between elevation and surface water mass, another data set better illustrates the transitions between normal, drought, and wetter periods in California and the western United States. The Palmer Drought Severity Index (PDSI) is a measure that reflects whether a region is experiencing drought or wet period (Dai, 2011; Palmer, 1965). The PDSI is available monthly from year 1895 to the present, is seasonally adjusted, and is derived from meteorological data such as precipitation and temperature. It represents the departure from normal conditions in given region, expressing the balance between *supply* and *demand* of water, but does not include man-made changes, for example, in reservoir or aquifer management. The values vary from −7 representing extremely dry to +7 extremely wet conditions, with about 90% of values lying within ±4. We obtained data for the Western United States, California, and Great Basin regions from NOAA National Centers for

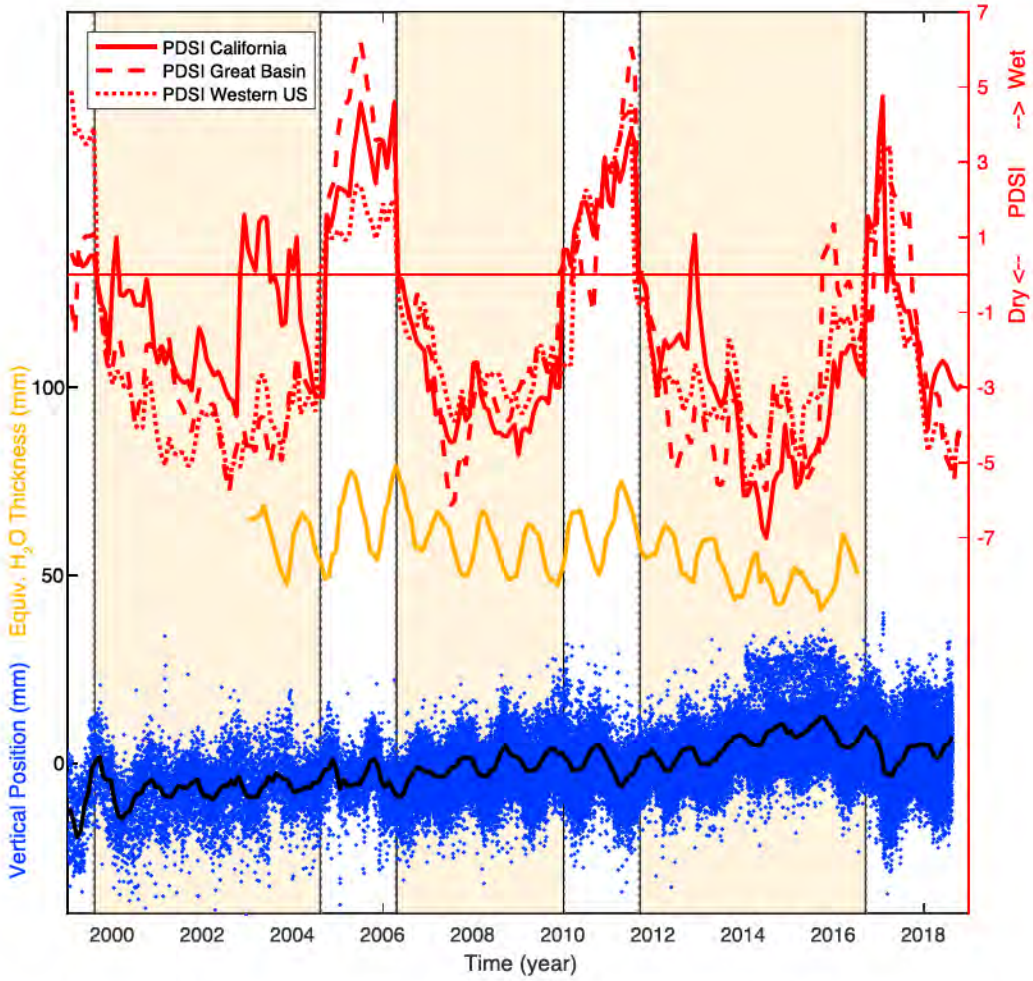

Figure 3. Comparison between indicators of drought versus wet periods to GPS uplift data. Red lines show monthly values of Palmer Drought Severity Index (PDSI) for California, Great Basin, and Western U.S. (referring to scale on right vertical axis). Orange line shows GRACE Mascon #1895 in mm of H_2O equivalent water thickness (referring to scale on left vertical axis). Blue dots are summary of Sierra Nevada west slope GPS stations vertical positions as plotted in Figure 1, with monthly means in black (referring to scale on left vertical axis). The time series are shifted vertically to increase clarity.

Environmental Information (ftp://ftp.ncdc.noaa.gov/pub/data/cirs), plotting values between 1999.0 and the present (Figure 3).

Swings in the PDSI between 1999 and the present indicate the dryer than average periods, what are termed *droughts*, between 2000–2004, 2006–2010, and 2012 to mid-2016, with the latest period experiencing the most intense drought, with PDSI = −7 in June 2014. These periods are correlated with especially rapid GPS-measured uplift and the intervening wet periods with the intermittent drops in elevation (Figure 3). We focus on the times when PDSI changed from positive to negative and subsequently vice versa and adopt the interval 2011.7 to 2016.7 to represent the recent drought period.

4. Results

4.1. Average Deformation 1996.0–2018.5

The horizontal velocity vectors obtained using MIDAS show first-order properties similar to previous results, where velocities in a North America reference frame increase westward from ~4 mm/yr in the eastern Walker Lane to ~12 mm/yr near the Sierra Nevada crest (Figure 4a). The velocities diverge at the LVC in response to magmatic inflation and are superimposed on the background tectonic shear (Figure 4a). The

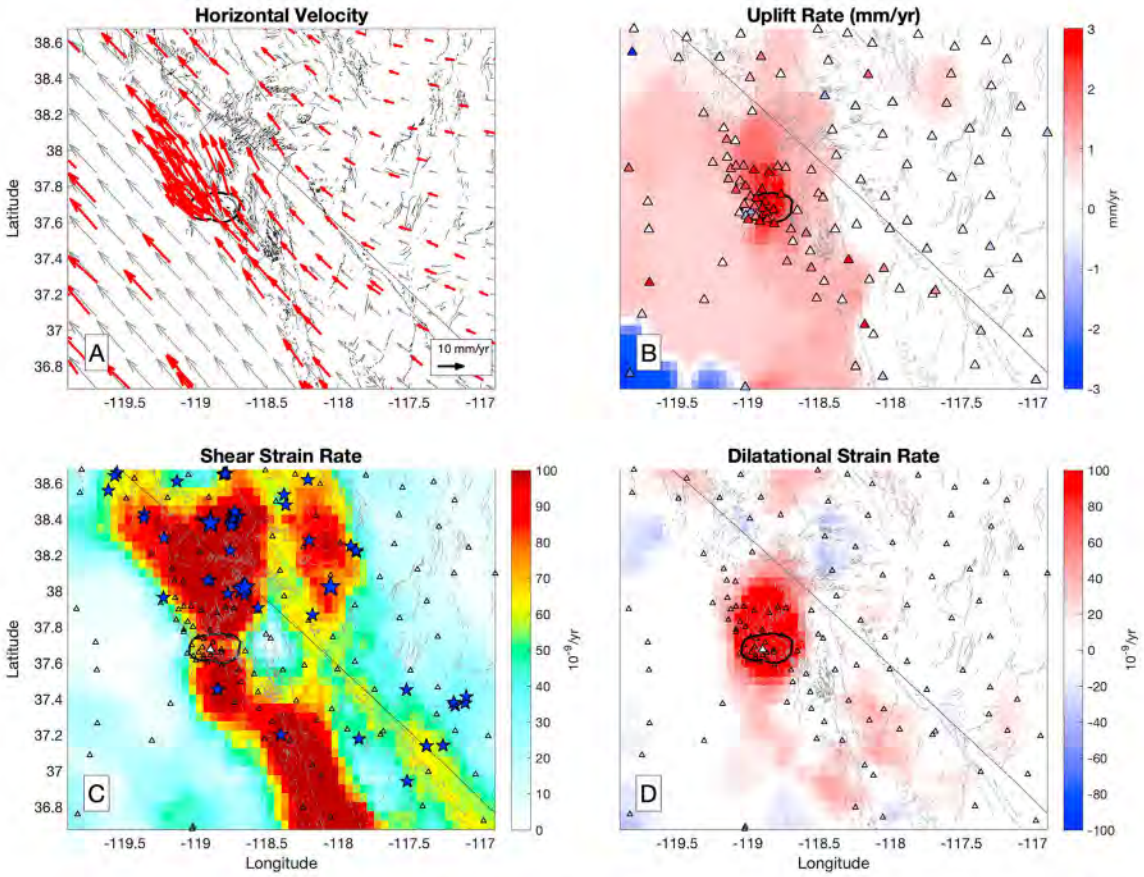

Figure 4. (a) Horizontal GPS velocities for the entire GPS dataset 1996.0 to the present. Gray lines are Quaternary faults. Black outline is location of LVC. Gray vectors are interpolated from the red vectors using GPS Imaging. (b) Uplift rate from GPS Imaging, vertical rate at each station is shown with triangle color. (c) Shear strain rate. Blue stars are epicenter locations for earthquakes above *M*4, larger stars if $M \geq 5$, for events occurring in years 2000.0–2018.0, the period of the seismicity analysis (see Discussion for details). (d) Dilatational strain rate. In this and in the following figures the black northwest-southeast diagonal line is the California/Nevada border.

uplift rate on the west slope of the Sierra Nevada is ~1 mm/yr and is much higher (around 5 mm/yr) at the LVC (Figure 4b).

From the gridded tensor strain rate components determined using the method described above, we present the principal strain rates $e\cdot_1$ and $e\cdot_2$ and then separately plot the shear component (which we define here as $e\cdot_1 - e\cdot_2$, Figure 4c) and the dilatational component ($e\cdot_1 + e\cdot_2$, Figure 4d). The resulting image shows that the highest values of CWL shear strain rate are immediately adjacent to the Sierra Nevada, in the westernmost CWL and in the Owen's Valley. While this is similar to previous results, this new imaging shows more confinement of the highest shear strain rates through the location of the LVC. To the north of the LVC, shear strain rates are more broadly distributed between the Sierra Nevada range front and the Wassuk Range/Benton Springs fault zones on the eastern edge of the Walker Lane, where part of the strain budget seems to step eastward, through the Mina Deflection (Wesnousky, 2005). The dilatation rates (Figure 4d) reveal that the dominant source of crustal extension is directly at the LVC, but some slower extension also exists in the CWL to the north and southeast of LVC. The results suggest that decomposition of the tensor strain rate field into dilatation and shear components effectively separates the signals of CWL tectonic shear deformation from the signature of transient magmatic inflation. A weak zone of dilatation between longitude −118.5° and −118° at latitude 37.2° exists near the Deep Springs fault zone, a northeast striking normal fault east of Owens Valley with a slip rate less than 1 mm/yr (Lee et al., 2001).

4.2. Deformation Prior to, and During, the Drought

To clarify the impact of time variability in the uplift and strain rate fields, we split the GPS data set into early and late periods and repeat the imaging. The early period contains all data before the drought period that

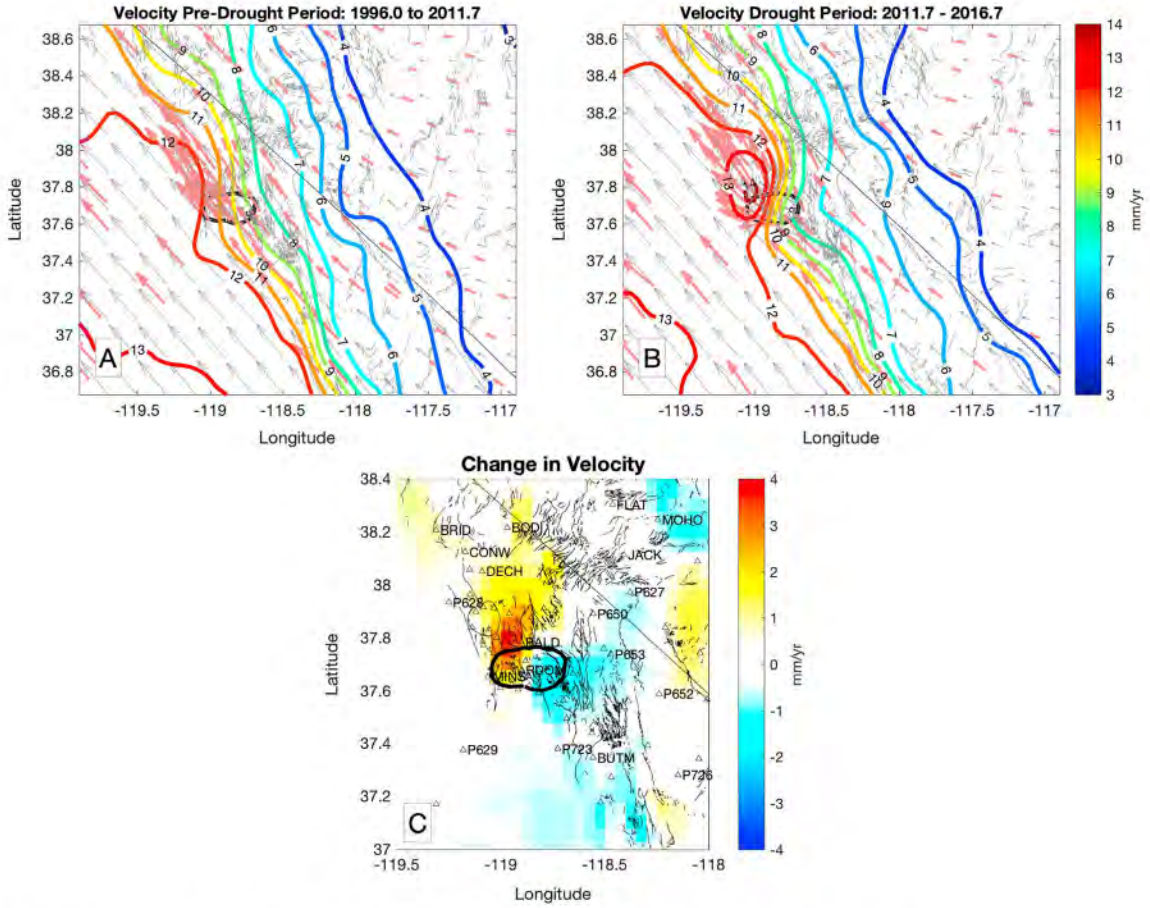

Figure 5. (a) GPS horizontal velocity before year 2011.7. Light red vectors are velocities at GPS stations, and gray vectors are decimated gridded version of those used to generate color contours of velocity magnitude at levels of 1 mm/yr. Gray lines are Quaternary faults. Black outline is location of LVC. (b) Same as a except GPS velocity during the drought 2011.7 to 2016.7. (c) Color-shaded plot of change in GPS velocity from predrought to drough period, zoomed in closer into LVC area. Triangles are locations of GPS stations, and names of selected stations are shown. Faults with black lines. Hot colors indicate increase in magnitude of GPS velocity, and cool colors indicate decrease, in mm/yr.

began in 2011.7, and the second period includes data after this time until 2016.7 when the PDSI increased to become positive again. When a GPS station has data in a time series that spans both time periods, we divide the time series into early and late intervals. For the imaging we only take resulting time series that have over 2.5 years of data. A consequence of splitting the data in this way is that the station distribution and spacing may not be the same in the early and late periods so differences in strain rate field may be partly attributable to changes in resolution over time. Figure 5a (b) is similar to Figure 4a except that the result of using data only for the predrought (drought) period are shown, and additionally, contours of the magnitude of imaged GPS velocity overly the velocity field. Of the stations considered, there are 386 with sufficient data in the early period and 315 with sufficient data in the later period (which has shorter duration), and 292 stations that have sufficient data in both periods.

4.2.1. Velocity Changes

The drought period horizontal velocities show substantial increase in divergence at the LVC compared to the predrought period. Figure 5c shows a color-shaded plot of the difference between the dry period and wet period velocity magnitude. There is an increase in velocity magnitude of 3.8 mm/yr to the north of, and a decrease of 1.7 mm/yr to the south of, the LVC. This is a result of magmatic inflation advancing and retarding the background tectonic crustal motion to the north and south, respectively. The difference in horizontal velocity is near zero at the Resurgent Dome (station RDOM), where the vertical rate change is maximum. This is expected because horizontal motion directly above a buried inflating source is zero (Lisowski, 2007; Mogi, 1958), and this is the signal highlighted in the change of velocity. At the 0.5-mm/yr

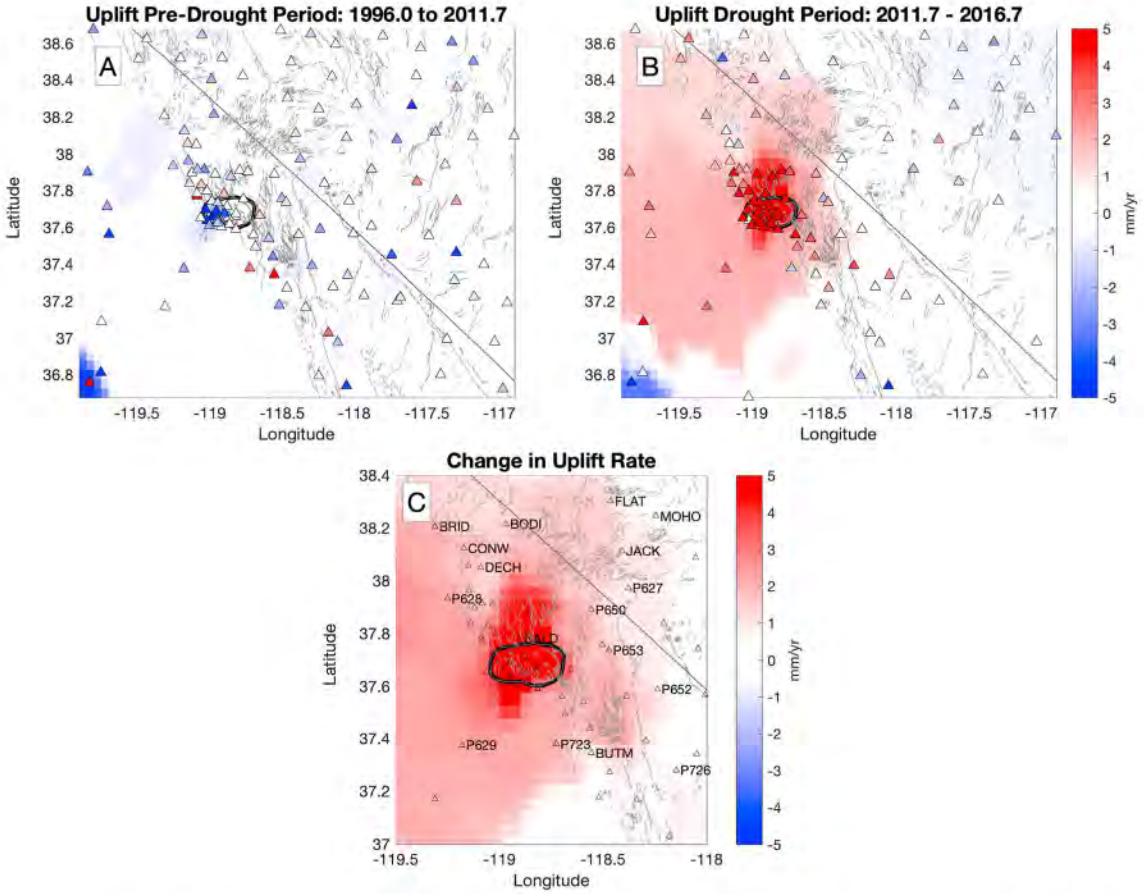

Figure 6. (a) GPS uplift rate before 2011.7. Color scale is in mm/yr. Triangles are locations of GPS stations used to estimate uplift field. Gray lines are Quaternary faults. Black outline is location of LVC. Vertical rate at each station is shown with face color of triangle. (b) GPS uplift rate 2011.7 to 2016.7. (c) Color-shaded plot of difference of GPS uplift rate, zoomed in closer to LVC.

level, which is near the level of uncertainty for changes in GPS rates for these truncated time series, the velocity changes are resolvable from Conway summit (near station CONW) and Bodi (station BODI) about 60 km north of the LVC (Figure 5c). To the south, changes as great as 0.5 mm/yr do not extend as far, reaching only about 30 km, about halfway to Bishop, CA, and the difference field there is discontinuous. In areas to the east, in Nevada there are two north-south striking areas of velocity difference near 0.5 mm/yr. These may be artifacts attributable to changes in data availability and GPS station distribution between the early and late periods and that this area lacks continuous stations. However, the north-south asymmetry in the velocity change field around LVC is well resolved. The velocity change in the vicinity of the Mono-Inyo Crater chain is greater and more extensive, compared to the velocity changes near Mammoth Crest to Wheeler Crest area in the Sierra Nevada to the south. This is similar to the findings of Marshall et al. (1997) and Feng and Newman (2009) who both detected roughly east-west extension across this area during different inflationary episodes, interpreting it as opening in a north-striking dike extending from LVC toward the Mono-Inyo Crater chain. This analysis suggests that this same structure may be active during the recent inflation period.

Figure 6 shows the early and late periods of uplift from the vertical GPS time series split into the early and drought periods. The predrought period shows a nonuplifting or subsiding Sierra Nevada (Figure 6a). There is a minor amount of focused subsidence inside the LVC suggesting a deflationary tendency during the pre-drought period. In contrast, the drought period shows uplift everywhere on the Sierra Nevada west slope (Figure 6b) and even more rapid uplift at LVC (~13 mm/yr). The difference between the drought and pre-drought images (Figures 6c) shows the acceleration of uplift. Like the horizontal measurements the change in uplift rate is asymmetric, extending at the 1-mm/yr level farther to the north, nearly to Conway summit

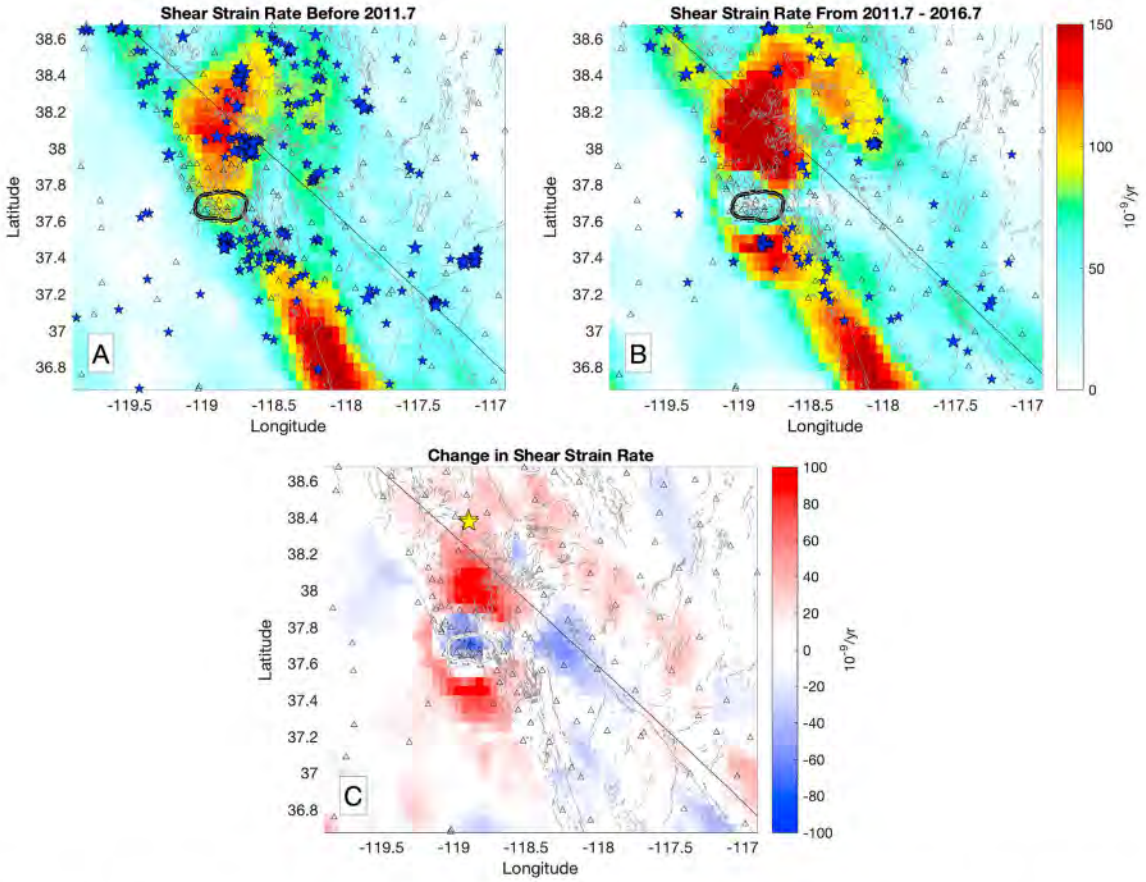

Figure 7. (a) Shear strain rate before 2011.7. Color scale is in 10^{-9} per year. Triangles are locations of GPS stations used to estimate shear strain rate field. Black outline is location of LVC. Gray lines are Quaternary faults. White triangles are earthquake epicenters for events with M3–4 (small stars) and $M > 4$ (larger stars). (b) Shear strain rate from 2011.7 to 2016.7. Symbols as in a. (c) Difference in shear strain rate from wet to dry period. Yellow stars indicate location of the three Nine Mile Ranch earthquakes over M5.5 that occurred in December 2016.

and Bodie, and to the south as far to Bishop. The change in uplift rate is not confined to the LVC or Sierra Nevada but extends east of the Sierra crest into Nevada.

4.2.2. Strain Rate Changes

Using the method described above, we calculate strain rate fields for both predrought and drought periods. The differences between them show how the strain rate in the CWL was affected by LVC inflation during the drought. Figure 7 shows the shear strain rate and Figure 8 the dilatational strain rate in each period. During the drought the strain rates increased north and south of the LVC and decreased to the east and west. The observed horizontal dilatation rate changed from weak expansion to vigorous expansion during the drought (Figure 8), consistent with the interpretation as magmatic inflation (Montgomery-Brown et al., 2015). The change is mostly contained in the compact circular zone where GPS Imaging locates the dilatation, but also, there are lobes of contraction to the northeast, southwest, and southeast of the main anomaly. As with the changes in velocity shown in Figures 5 and 6, the center of the change is slightly north of the LVC.

A number of studies sought to quantify the crustal strain rates in the Great Basin/Sierra Nevada transition near LVC (e.g., Hammond & Thatcher, 2007; Kreemer et al., 2012; Lifton et al., 2013; Oldow et al., 2001). Here we are imaging the strain rate field twice with separate data sets, providing an opportunity for signals seen in both data sets to corroborate one another. Also, we can assess uncertainties in the imaged fields by inspecting profiles of the velocity images along lines oriented northeast/southwest across the CWL (Figure 9). These profiles show the magnitude of velocity changes compared to the uncertainties in the individual velocities and how the velocity imaging is robust to outliers. Furthermore, the strain rate changes derived from the velocity images accurately reflect the changes in the gradients of the velocity fields. For example, we see in the northern profile an increase in shear strain rate near km 50 where the velocity

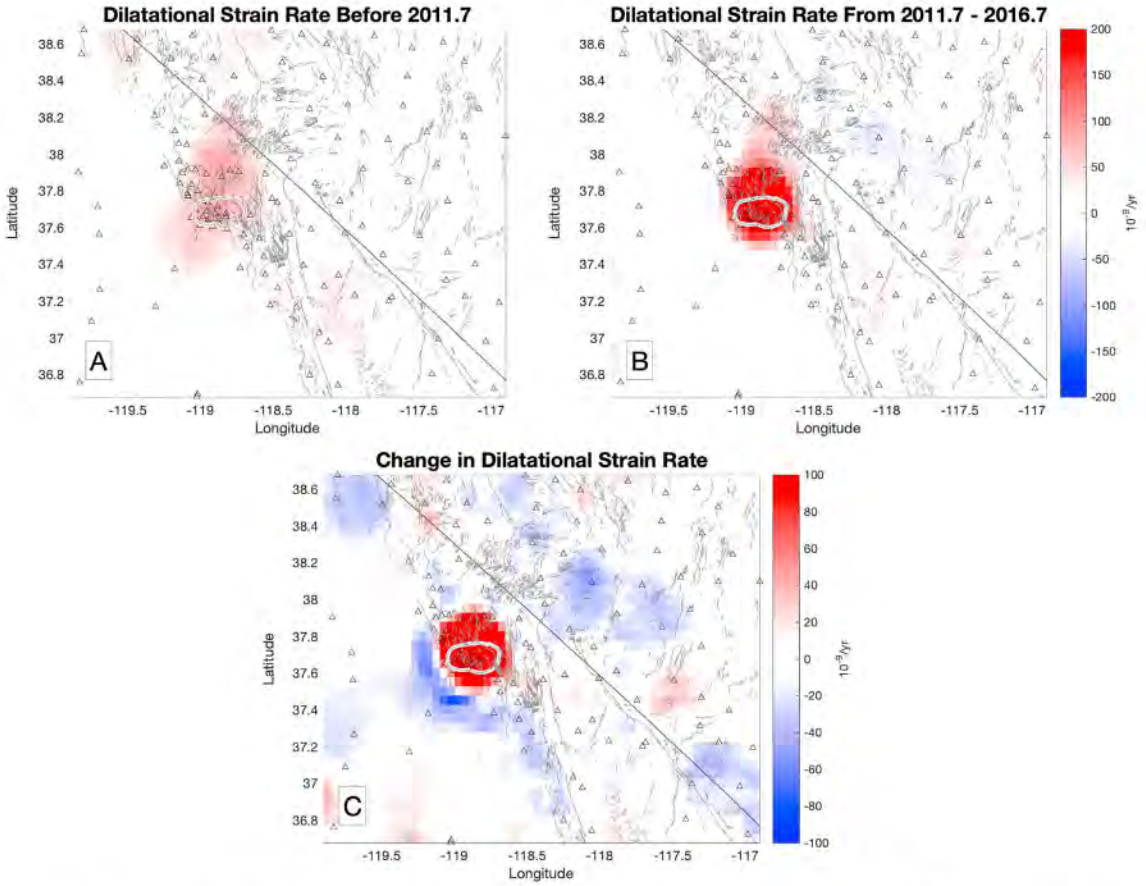

Figure 8. Dilatational strain rate (a) before 2011.7 and (b) during the drought period 2011.7 to 2016.7. Color scale is in 10^{-9} per year. Triangles are locations of GPS stations used to estimate strain rate field. White outline is location of LVC. Gray lines are Quaternary faults. (c) Difference in dilatation rate from early to later period.

magnitudes increase on the west end of the profile, consistent with Figure 5c. In general, the shear strain rate changes (Figure 7) are consistent with velocity changes plotted in Figure 5, and this is further supported by the profiles (Figure 9). The shear strain rate changes are large, nearly doubling from 1.5×10^{-7} per year to a maximum of 2.5×10^{-7} per year in the northern profile and from 0.9×10^{-7} to 1.5×10^{-7} per year in the southern profile.

5. Discussion

5.1. Is Long Valley Inflation Triggered by Drought?

Previous studies have shown a relationship between drought intervals and Sierra Nevada uplift that is primarily the result of terrestrial water storage and surface mass loading changes in the Sierra Nevada Mountains and California Central Valley aquifers (Amos et al., 2014; Argus et al., 2017). Here we point out that accelerated inflation of LVC also coincides with the inflection in Sierra Nevada uplift at year 2011.7 and has a larger amplitude. In Figure 10 we compare (1) the elevation change of GPS station RDOM that lies near the Resurgent Dome near the inferred center of magmatic inflation (Feng & Newman, 2009; Langbein et al., 1995), (2) the median uplift for all stations in the LVC, and (3) the stacked uplift of the west slope of the Sierra Nevada. In response to inflation the station RDOM rose ~80 mm between 2011 and 2016, about 8 times more than the Sierra Nevada rose. To maximize robustness of the vertical signal of inflation, we additionally look at data from the set of 25 stations nearest RDOM. We destep and shift the time series together with the same procedure used to make Figure 2a and then take monthly medians. Against these, we compare monthly medians of positions for the destepped and shifted stack of nine stations on the Sierra Nevada west slope nearest the LVC (Figure 10).

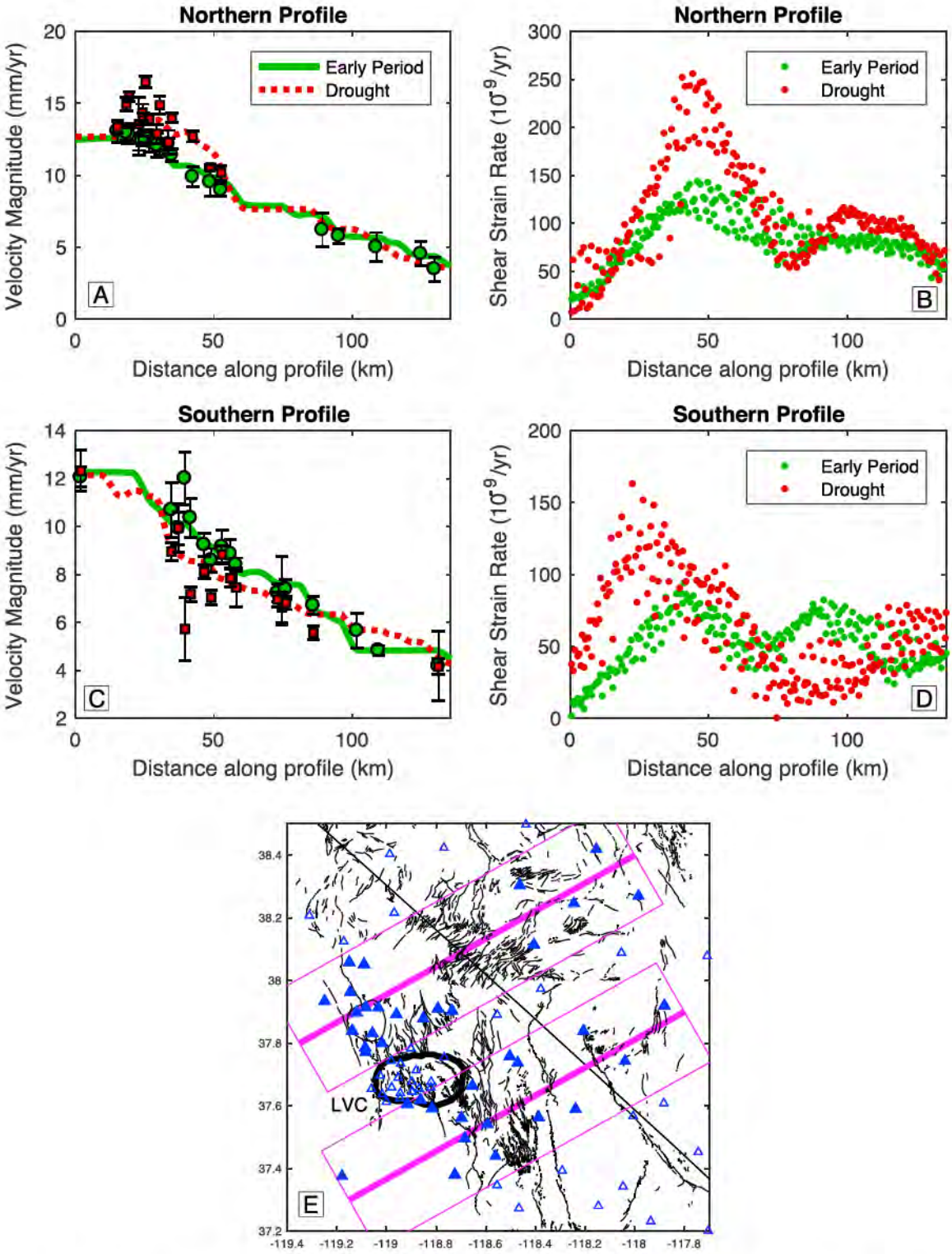

Figure 9. GPS velocity, imaged velocity, and shear strain rate in two profiles, one north and one south of the LVC. (a) and (b) are northern profile, (c) and (d) southern profile. In (a) and (c) velocity (circles and squares) and imaged velocity (solid lines) are shown together. (b) and (d) are profiles of imaged shear strain rate at all grid points that lie within the profile bounds (magenta boxes in e). (e) Location of profiles on same map bounds as previous figures. Black outline is location of LVC. Black lines are Quaternary faults. Blue triangles are GPS stations that are filled for stations within the profile bounding boxes.

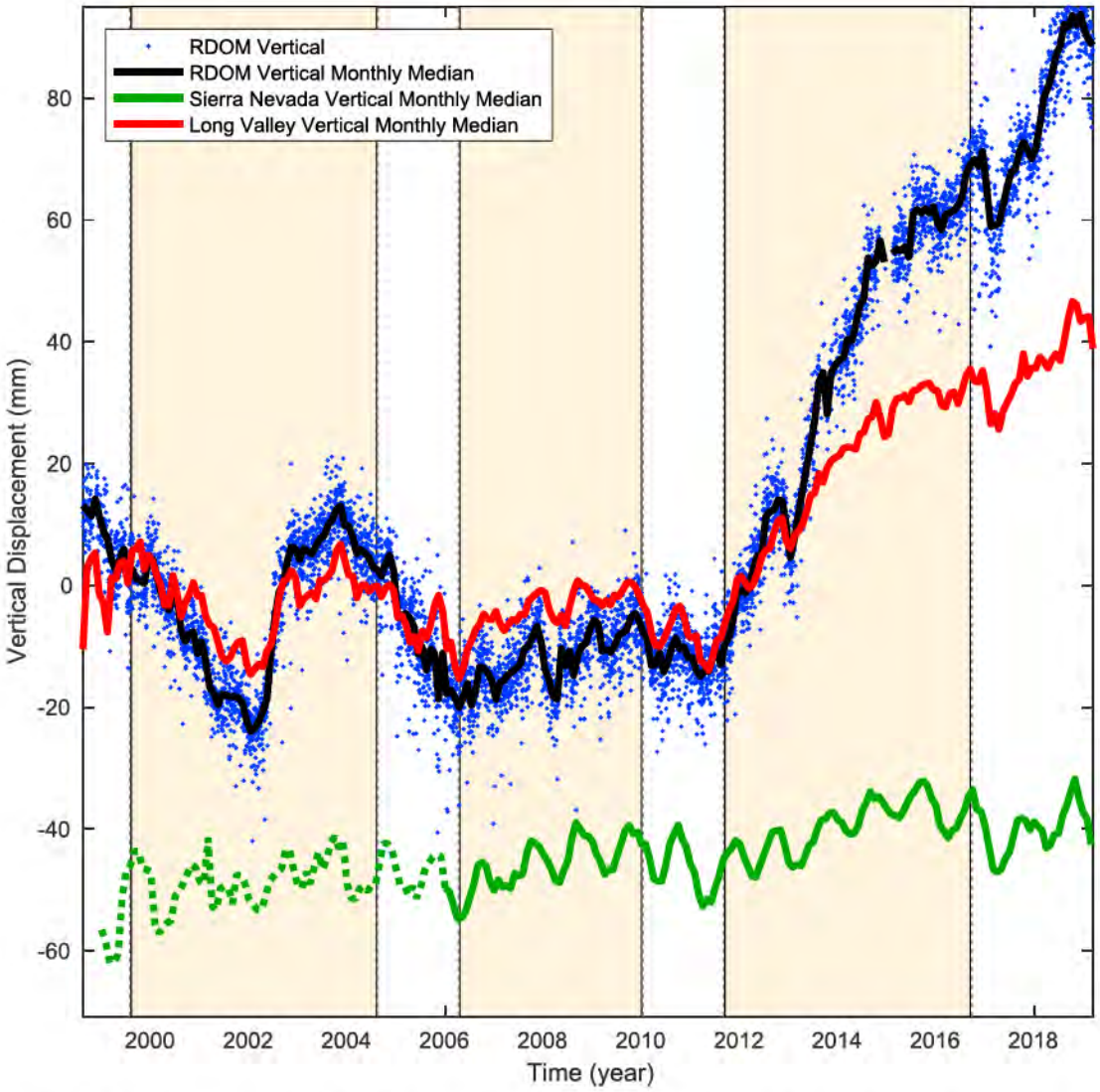

Figure 10. Time series of GPS station RDOM (blue dots) and its monthly median (black line), compared to monthly medians of positions from 25 stations in the LVC (red line), and to change in elevation of west slope of Sierra Nevada using nine stations nearest and west of LVC (green line). There are fewer stations to constrain Sierra Nevada uplift before 2006 (Figure 2), so the green line is dotted to indicate greater uncertainty. Drought intervals in California are indicated with light colored shading as in Figure 3.

The comparison shows strong correlations between the drought-enhanced uplift of the Sierra Nevada and the accelerated uplift of RDOM and LVC, between 2011.5 and 2016.5. All time series show the same inflection in uplift near 2011.7, near the beginning of the recent drought period. They each exhibit the up-then-down vertical motion between 2006 and 2011. They also show similarities in the seasonal motions, with in-phase vertical oscillation of all three time series. We also see similar year-to-year changes in seasonal amplitude, such as during the winter of 2016–2017 (a very heavy precipitation season, with nearly double normal snowpack in the Sierra Nevada), when an especially large downward dip is observed. One difference is that after the very heavy 2016/2017 precipitation season, the LVC uplift seems to continue until the present, though at a lower rate compared to middrought, whereas the Sierra Nevada uplift may have entered a subsidence stage.

The similarities in these time series invite speculation about the causal relationship between Sierra Nevada uplift and LVC inflation. A straightforward conjecture is that LVC magmatic inflation is responding to the same loading that drives Sierra Nevada elevation changes. Alternatively, LVC inflation could be responding the stress changes derived through the intermediary vertical motion of the Sierra Nevada. In either case the

load footprint size is on the scale of at least the Sierra Nevada seasonal snowpack, extending hundreds of kilometers north and south of LVC, though in the latter case it lies 10–20 km west of the LVC. It is also important to notice that the seasonal oscillations and the transient uplift between 2006 and 2011 are similar in magnitude between the Sierra Nevada and LVC, while the changes in vertical trends after 2011 are much greater for RDOM and LVC than for the Sierra Nevada. Thus, the seasonal LVC signal probably represents the same direct response to loading that is seen in Sierra Nevada stations. However, the inflation events (e.g., the big increase in upward trends for the black and red curves at 2011.7) are attributable to the acceleration of a process somewhere in the LVC magmatic system that is responding to nonseasonal changes in hydrological unloading.

Episodes of inflation and deflation before 2006 are not perfectly correlated with Sierra Nevada uplift. However, before 2006 there were far fewer Sierra Nevada GPS stations so geographic coverage and resolution were poorer (Figure 2). So there may have been a correlation between Sierra Nevada and transient RDOM/LVC uplift during 2002–2006, but it was not well resolved. It is also clear that not all episodes of LVC inflation are related to drought. We can see from the PDSI time series that goes back to 1975, a period prior to GPS monitoring but covered by EDM, leveling, and seismicity monitoring, that the correlation between PDSI and inflation periods was not strong (Hill, 2006; supporting information Figure S2). Thus, hydrological unloading is not the only control on inflation. However, it can on some occasions effect timing of inflation initiation that was otherwise physically ready to occur.

The suggestion that a drying climate can influence loading conditions that modulate magmatic inflation and volcanism has precedent in various contexts and timescales. In Iceland, for example, cases have been documented where productivity, timing, and chemistry of volcanic eruptions are linked to recession of glaciers (Gee et al., 1998; Jull & McKenzie, 1996; Maclennan et al., 2002; Sigmundsson et al., 2017; Sigvaldason et al., 1992) or as snowpack changed seasonally (Grapenthin et al., 2006). In eastern California comparison of the timing of eruptions with the global record of glacier growth and retreat over the last 400 kyr suggests a connection between glacial unloading and eruptions (Jellinek et al., 2004). While these examples describe loading changes orders of magnitude larger than the changes in Sierra snow load discussed here, they do provide some plausibility for a mechanism where surface pressure changes can affect the LVC magmatic system at depth. However, even simple models of magmatic systems are complex, with plumbing that may be vertically and horizontally extensive, with multiple zones and styles and interconnectivity of fluid containment (Cashman et al., 2017; Hill, 2006; Lowenstern et al., 2017), and processes controlled by many geometric, physical, and chemical parameters (e.g., Anderson & Segall, 2011). As a result it is difficult to know how, and what part of, the LVC system is responding to surface pressure changes.

5.2. Inflation-Driven Deformation of the Central Walker Lane

The changes in the strain rate field found using GPS Imaging reveal with new detail how the CWL crust around the LVC responds to the presence of an inflationary body near the Sierra Nevada/western Great Basin transition. Among these, we see shear strain rate changes that increase north and south of LVC and decrease to the east. West of LVC the GPS station coverage is poor in the Sierra Nevada high country, which is dominated by wilderness areas, but there is a hint of contraction, which has smeared to the northwest of LVC (Figure 7c). These changes in strain rate are consistent with the expectation based on a simple kinematic model of an inflationary source within a shear field, as has been observed at other magmatically active transtensional plate boundaries (Sigmundsson et al., 1997). To illustrate this, we have constructed a model velocity field based on LVC inflation inside constant northwest directed CWL tectonic shear (Figure 11a). The shear is represented by a northeast to southwest gradient in northwest velocity of 10 mm/yr, similar to the Walker Lane except with constant strain rate. Superimposed on that is the velocity expected from an inflating 1-km radius, 7-km deep spherical inflationary Mogi source (Lisowski, 2007) scaled to provide radial rate similar to what we found for LVC (2.8 mm/yr). We then mimic the analysis used to make Figure 7c, calculating shear strain rate from this synthetic velocity field and then subtracting the shear strain rate from the velocities without the inflationary component (simulating predrought conditions). The result (Figure 11b) shows where shear strain rates increase (north and south of LVC) and decreases (east and west of LVC), similar to the strain rate changes shown in Figure 7c.

This is the expected pattern because shear strain rates are the difference between greatest and least principal strain rates, so inflation-driven contraction north and south of LVC enhances shear, while reduced

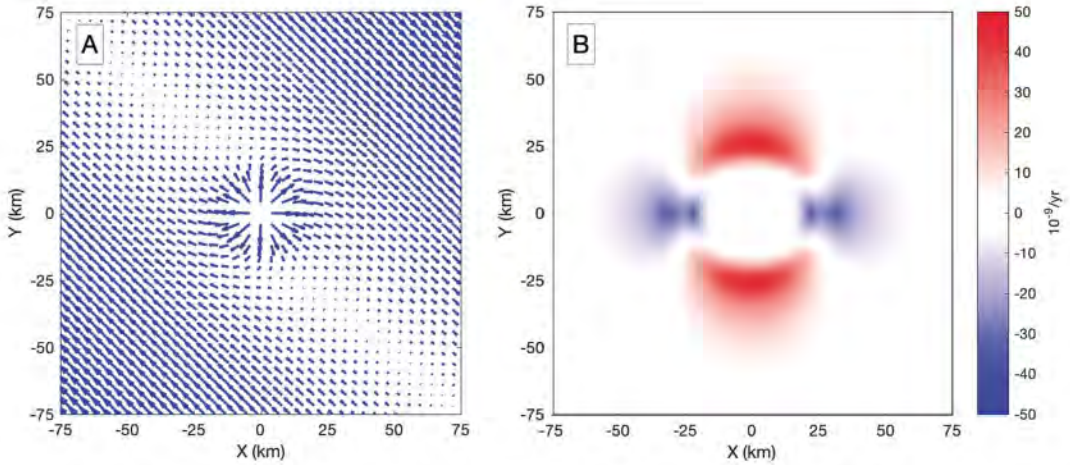

Figure 11. (a) The velocity pattern from a superposition of Mogi inflation plus a constant shear strain rate similar to LVC in the CWL. The velocity field is actually 4 times as dense as indicated but is decimated for plotting. (b) The change in shear strain rate between the velocities shown in (a) and a similar model with the inflation removed; see text for details.

extension to the east and west reduces shear. There is a lack of 90° rotational symmetry in the shear strain rate change field because of the bias that shear strain rates have toward being positive values since they are defined here as the difference between larger and smaller principal strain rates. The match between Figures 11b and strain changes in Figure 7c is not perfect, but differences can be explained by the facts that (1) GPS Imaging resolution is limited, (2) the inflationary source may not be perfectly spherical, and (3) the background CWL tectonic strain is not geographically uniform (Figure 4c).

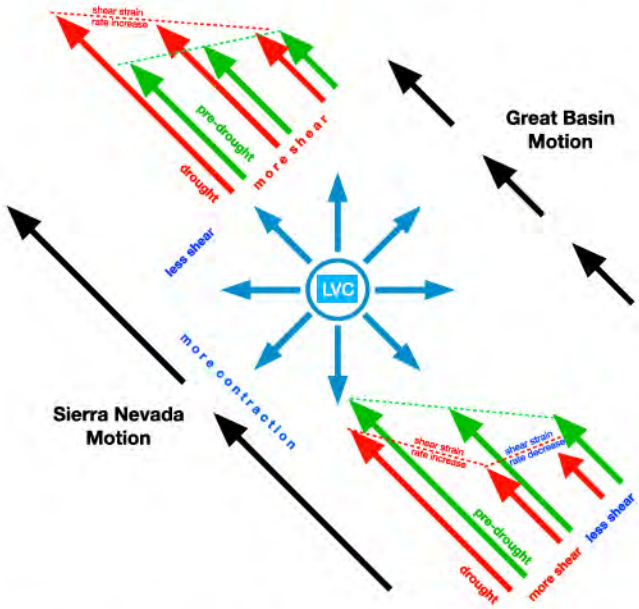

Figure 12. Cartoon model of crustal shear deformation in the presence of an inflationary source near a right step in the Walker Lane fault system. Simplified time-invariant far-field motion of the Sierra Nevada and Great Basin is shown with black vectors. LVC inflation is indicated with blue vectors. Shear deformation in the CWL is shown both prior to the drought period (green vectors) and during the drought period (red vectors). The changes in lengths of these vectors resulting from LVC inflation change the distribution of shear and dilatational deformation in the CWL. Dashed lines help to visualize gradients in velocity and how they change between pre-drought and drought periods.

This strain rate changes can be further illustrated in a slightly more realistic cartoon model by considering changes in motion from an inflationary source sitting within a right step in the shear field (Figure 12). In this model, northwest of LVC the inflation accelerates the west side of the northwest directed CWL shear, enhancing the shear strain rate. On the southeast side of LVC, the inflation pushes southeast, slowing down the velocity near the middle of the profile, decreasing the shear strain rate on the east side of the CWL and increasing it to the west. This is observed in the pattern of change in the shear strain rate and helps explain some of the differences between the very simple model in Figure 11 and imaged strain rate in Figure 7c.

The observed changes in the dilatational strain rate show a positive signal at LVC but also negative dilatation in its periphery to the west and south (Figure 8c). Peripheral negative dilatation is an expected consequence of inflation from a deep expanding body pushing outward into adjacent areas (Lisowski, 2007; Mogi, 1958). While it is found in our images, its geographic resolution is limited by sparse GPS station distribution west of LVC in the Sierra Nevada. In contrast, to the north and east of LVC the negative dilatation is absent, even though GPS stations are present. We speculate that this could be because the CWL to the east and north of LVC has different crustal properties than the Sierra Nevada and responds to nearby LVC inflation with a less focused negative dilatation. The CWL crust could be weaker or less bounded than that of the Sierra Nevada, that is, free to move away so that this strain does not accumulate near to the LVC.

5.3. Drought Quakes in the Central Walker Lane?

Recent studies have identified a connection between loading-induced strain and earthquake rates in Nevada and California (e.g., Johnson

Table 1
Number and Rate of Seismic Events in Zones of Increased and Decreased Shear Strain Rate

Number of Events

	Where strain rate		Where strain rate was		
	Decreased	Increased	High	Low	All places
Wet period	479 (21.9)[a]	939 (30.6)	1,491 (38.6)	878 (29.6)	2,369 (48.7)
Drought period	193 (13.9)	395 (19.9)	636 (25.2)	339 (18.4)	975 (31.2)
All times	672 (25.9)	1,334 (36.5)	2,127 (46.1)	1,217 (34.9)	3,344 (57.8)

Events per Year

	Where strain rate		Where strain rate was		
	Decreased	Increased	High	Low	All places
Wet period	41 (1.9)	80 (2.6)	127 (3.3)	75 (2.5)	202 (4.2)
Drought period	39 (2.8)	79 (4.0)	127 (5.0)	68 (3.7)	195 (6.2)
All times	40 (1.6)	80 (2.2)	127 (2.8)	73 (2.1)	200 (3.5)

[a]The values in parentheses indicate standard deviations of the reported numbers/rates under assumption of a stationary Poisson point process with the same event rate.

et al., 2017; Kreemer & Zaliapin, 2018). Here we investigate seismicity rates in our study area to determine if they are sensitive to the horizontal strain rate changes associated with the drought periods. In Figure 4 we plotted the locations of all earthquakes with $M > 4$ over our map of strain rate. This shows a general tendency for earthquakes to occur more frequently in the areas where strain rates are highest, similar to expectation. This tendency holds for both the predrought and drought periods (Figures 7a and 7b) and also holds for microseismicity, which we show next.

In the supporting information we show how we use the method of Zaliapin and Ben-Zion (2013) to decluster and evaluate completeness of a catalog of seismicity for the part of our study area that lies outside of the LVC. From this catalog we count background earthquakes and estimate background seismicity rates in subsets of the data. We define two geographic areas based on whether the shear strain rate (Figures 7a and 7b) increased or decreased during the drought (Figure 7c). We ignore events within a transition zone where the absolute value of the strain rate change was less than 10^{-8} per year (the approximate uncertainty in the strain rate estimation). The resulting two domains are where strain rate changed significantly, either positively or negatively, and they are approximately equal in area. We then divide our list of background earthquakes into two separate groups based on time, whether the event occurred before or during the drought period (2011.7–2016.7). With these assignments we can then categorize each event into one of four separate groups, distinguished by when and where the event occurred. We count the number of events that occurred in each bin and divide by the number of years in each temporal bin to obtain the rate of earthquakes in each category (Table 1). Additionally, we separate the domain into areas where background tectonic strain rate greater than or less than 4×10^{-8} per year (Table 1).

In this analysis a number of choices are made that determine into which bins earthquakes fall. We tested many different choices that had small effects on the earthquake counts. For example, the time considered as the drought period could be adjusted to include all times with PDSI <0, which places more earthquakes in dry times and fewer in wet times (Figure 3). Also, we tried different parameterizations of the strain rate, which slightly changes the geographic bins earthquakes fall into. For example, we tried shear strain rate domains defined as the minimum absolute value of principal strain rates ($\min(|\dot{e}_1|, |\dot{e}_2|)$), dilatation strain rate ($\dot{e}_1 + \dot{e}_2$), and magnitude of strain rate $\left(\dot{e}^2_{\phi\phi} + \dot{e}^2_{\theta\theta} + 2\dot{e}^2_{\phi\theta}\right)^{1/2}$, where $\dot{e}_1, \dot{e}_2$ are the principal strain rates derived in section 4.2.2, as alternatives to the shear strain rates shown in Figures 4 and 7. These choices change the numbers of events in each bin. We report below on one set representative assumptions and focus our discussion on properties that are insensitive to changes in them.

The results indicate some features that were expected and others that were not. First, as expected, seismicity rates were much larger in areas where strain rates were higher (127 ± 2.8 per year in high strain rate areas compared to 73 ± 2.1 per year in low strain rate areas, Table 1). Also, we see that in areas where the strain

rate increased during the drought period, the seismicity rate was twice as large as other areas (80 ± 2.2 per year compared to 40 ± 1.6 per year). However, we see that the strain rate is larger in these areas for both the early and drought periods. In other words, the seismicity rates did not increase during the drought period. Inside the zone where shear strain rates decreased, the background seismicity rate did not change significantly (41 ± 1.9 to 39 ± 2.8 per year), nor did they change in places where strain rates increased during the drought (80 ± 2.6 to 79 ± 4.0 per year). For all areas, the seismicity rate between wet and dry periods did not significantly change (202 ± 4.2 to 195 ± 6.2 per year). Thus, the spatial signals of seismicity distribution correlating with strain rate are strong, but the temporal signals are not.

The fact that the area where strain rate increased during drought happens to be the area that already had a high tectonic strain rate may not be a coincidence. For example, the presence of LVC may have helped to influence where the higher CWL strain rates occur. The GPS Imaging of strain rate and its changes (Figures 4 and 7) show that the highest strain rates are near the eastern margin of the Sierra Nevada, western edge of the CWL, and pass directly through LVC. Furthermore, while inflation is usually regarded as a transient signal and not a feature of the long-term crustal deformation field, LVC inflation tends to inflate but not subsequently deflate fully. Instead, it tends to progressively increase its total inflationary volume over time, at least over the recent decades of leveling and EDM monitoring (e.g., Battaglia et al., 2003; Hill, 2006; Langbein, 2003; supporting information Figure S2). Thus, the inflation-driven strain seen in Figure 7 may be a continuing and important, albeit unsteady, component of the cumulative accumulation of strain in the CWL. One possibility is that the unsteady inflation helps weaken the crust in areas it strains, attracting long-term deformation to occur there and driving enhanced seismicity. During the recent episode the inflation-driven strain at LVC contributed deformation at rates similar to those from tectonics, for example, as seen in Figure 5, up to ~3–4 mm/yr outside the caldera. Thus, it may not be correct to model and remove inflation-driven strain from the CWL velocity field before using the geodetic data for estimating slip rates that are valid over the long term. This observation has implications for geodetic fault slip rate studies outside but near LVC (e.g., Bormann et al., 2016; Dixon et al., 2003; Zeng & Shen, 2014).

A significant fraction of the total earthquake moment released in the study area over this time occurred on 28 December 2016, Nine Mile Ranch sequence southwest of Hawthorne, Nevada. In this sequence three moderate-sized strike-slip events (M5.6, M5.5, and M5.6) occurred within 1 hr of one another inside the area where the shear strain rate increased during the drought period (Figure 7c). The events had strike-slip mechanisms with near-vertical nodal planes striking 206°/308°, 213°/311°, and 210°/300° (Hatch et al., 2017), making their coseismic slip consistent with tectonic shear accumulation in the CWL (Hammond & Thatcher, 2007) in addition to the acceleration in shear strain accumulation induced by inflation (Figures 11 and 12). Thus, these events may represent examples of how regional tectonics and LVC inflation collude to drive deformation and earthquakes at distances >60 km from LVC.

6. Conclusions

We use GPS data to show how the timing of a recent episode of inflation of the magmatic system at the LVC is correlated with the initiation of the recent drought period in California. This episode of inflation, which began in late 2011 and continues to the present, coincided with a period with higher Sierra Nevada uplift rates and when the CWL experienced anomalous horizontal crustal shear strain rate patterns. The timing of drought is derived from the Palmer Drought Severity Index and GRACE satellite data, which point to drought-induced unloading of the Sierra Nevada during this period. This analysis illustrates links between climate, a large silicic magmatic system, active tectonics, and CWL earthquakes.

The changes in horizontal GPS velocity are geographically extensive and strongly asymmetric to the north and south, extending at least 60 km north to Bodi, CA, but to a lesser distance to the south, about 30 km. This asymmetry is consistent with possible dike expansion between LVC and the Mono-Inyo Craters chain, as seen in earlier studies of earlier inflation episodes.

GPS Imaging of strain rate and its changes show that the highest strain rates are near the eastern margin of the Sierra Nevada and western edge of the CWL and pass directly through LVC. Moreover, the distribution of seismicity shows that more earthquakes occurred in areas with higher strain rates and in areas where the strain rates increased during inflation. Seismicity rates are higher in these locations whether inflation

episodes are occurring or not. This suggests that inflation-driven crustal strain may be a part of the long-term CWL strain accumulation near LVC.

The 28 December 2016 Nine Mile Ranch sequence southwest of Hawthorne, Nevada, had mechanisms consistent with Walker Lane tectonic strain accumulation but may have been additionally encouraged toward failure by stress changes related to accelerated inflation at LVC.

Acknowledgments
We thank UNAVCO for GPS data collection, data archiving, distribution, and hosting of software products for the EarthScope Plate Boundary Observatory and GAGE Facility, supported by the National Science Foundation awards EAR-0350028, EAR-0732947, and EAR-1261833. We thank the operators of the other GPS networks whose data were used in this study including the USGS, Washoe County, SOPAC, Caltech, U.S. Coast Guard, SmartNet North America, the Jet Propulsion Laboratory, UC Berkeley, and University of Wisconsin-Madison. The Jet Propulsion Laboratory supplied the GIPSY software and data products that we used in the GPS data processing. The results of the processing are GPS position time series, all of which are openly available via our website at http://geodesy.unr.edu. We obtained SRTM data using the Scripps GMTSAR tool (http://topex.ucsd.edu/gmtsar/demgen/) to make Figure 1. We obtained processed GRACE solutions using the MASCON browser tool from the Colorado Center for Astrodynamics Research (https://ccar.colorado.edu/grace/gsfc.html). We obtained seismicity data collected by Nevada Seismological Laboratory and Northern California Seismic System using the U.S. Geological Survey web services API (https://earthquake.usgs.gov/ws/). We used the GMT v5.4.1 software (Wessel et al., 2013) to generate Figures 1 and 2. We are grateful for support from NASA for projects NNX16AK89G and NSSC17K0565 and from the USGS NEHRP Program G17AP00004. GPS data acquisition in the MAGNET GPS network was supported by the USGS Geodetic Networks Program G10 AC00138 and G15 AC00078 and NSF-EAR projects 0635757, 0844389, and 1252210. This manuscript benefitted from discussions with Francesca Silverii, Emily Montgomery-Brown, and Brandon Schmandt who made helpful suggestions on the analysis and interpretation and from reviews by Freysteinn Sigmundsson and an anonymous reviewer.

References

Altamimi, Z., Collilieux, X., & Métivier, L. (2011). ITRF2008: An improved solution of the International Terrestrial Reference Frame. *Journal of Geodesy*, *85*(8), 457–473. https://doi.org/10.1007/s00190-011-0444-4

Amos, C. B., Audet, P., Hammond, W. C., Bürgmann, R., Johanson, I. A., & Blewitt, G. (2014). Uplift and seismicity driven by groundwater depletion in central California. *Nature*, *509*(7501), 483–486. https://doi.org/10.1038/nature13275

Anderson, K., & Segall, P. (2011). Physics-based models of ground deformation and extrusion rate at effusively erupting volcanoes. *Journal of Geophysical Research*, *116*, B07204. https://doi.org/10.1029/2010JB007939

Argus, D. F., Fu, Y., & Landerer, F. W. (2014). Seasonal variation in total water storage in California inferred from GPS observations of vertical land motion. *Geophysical Research Letters*, *41*, 1971–1980. https://doi.org/10.1002/2014GL059570

Argus, D. F., Landerer, F. W., Wiese, D. N., Martens, H. R., Fu, Y., Famiglietti, J. S., & Watkins, M. M. (2017). Sustained water loss in California's mountain ranges during severe drought from 2012 to 2015 inferred from GPS. *Journal of Geophysical Research: Solid Earth*, *122*, 10,559–10,585. https://doi.org/10.1002/2017JB014424

Battaglia, M., Roberts, M., & Segall, P. (1999). Magma intrusion beneath Long Valley Caldera confirmed by temporal changes in gravity. *Science*, *285*(5436), 2119–2122. https://doi.org/10.1126/science.285.5436.2119

Battaglia, M., Segall, P., Murray, J., Cervelli, P., & Langbein, J. (2003). The mechanics of unrest at Long Valley caldera, California: 1. Modeling the geometry of the source using GPS, leveling and two-color EDM data. *Journal of Volcanology and Geothermal Research*, *127*(3-4), 195–217. https://doi.org/10.1016/S0377-0273(03)00170-7

Bennett, R. A., Wernicke, B. P., Niemi, N. A., Friedrich, A. M., & Davis, J. L. (2003). Contemporary strain rates in the northern Basin and Range province from GPS data. *Tectonics*, *22*(2), 1008. https://doi.org/10.1029/2001TC001355

Blewitt, G., Hammond, W. C., & Kreemer, C. (2009). Geodetic constraints on contemporary deformation in the Northern Walker Lane: 1. Semi-permanent GPS strategy. In J. S. Oldow, & P. H. Cashman (Eds.), *Late Cenozoic Structure and Evolution of the Great Basin—Sierra Nevada Transition*, *Geological Society of America, Special Paper*, (Vol. 447, pp. 1–16). https://doi.org/10.1130/2009.2447(01)

Blewitt, G., Hammond, W. C., & Kreemer, C. (2018). Harnessing the GPS data explosion for interdisciplinary science. *Eos*, *99*. https://doi.org/10.1029/2018EO104623

Blewitt, G., Kreemer, C., Hammond, W. C., & Gazeaux, J. (2016). MIDAS trend estimator for accurate GPS station velocities without step detection. *Journal of Geophysical Research: Solid Earth*, *121*, 2054–2068. https://doi.org/10.1002/2015JB012552

Blewitt, G., Kreemer, C., Hammond, W. C., & Goldfarb, J. (2013). Terrestrial reference frame NA12 for crustal deformation studies in North America. *Journal of Geodynamics*, *72*, 11–24. https://doi.org/10.1016/j.jog.2013.08.004

Blewitt, G., Lavallée, D., Clarke, P., & Nurutdinov, K. (2001). A new global mode of Earth deformation: Seasonal cycle detected. *Science*, *294*(5550), 2342–2345. https://doi.org/10.1126/science.1065328

Bormann, J., Hammond, W. C., Kreemer, C., & Blewitt, G. (2016). Accommodation of missing shear strain in the Central Walker Lane, western North America: Constraints from dense GPS measurements. *Earth and Planetary Science Letters*, *440*, 169–177. https://doi.org/10.1016/j.epsl.2016.01.015

Borsa, A. A., Agnew, D. C., & Cayan, D. R. (2014). Ongoing drought-induced uplift in the western United States. *Science*, *345*(6204), 1587–1590. https://doi.org/10.1126/science.1260279

Cashman, K. V., Sparks, R. S. J., & Blundy, J. D. (2017). Vertically extensive and unstable magmatic systems: A unified view of igneous processes. *Science*, *355*(6331), eaag3055. https://doi.org/10.1126/science.aag3055

Dai, A. (2011). Characteristics and trends in various forms of the Palmer Drought Severity Index (PDSI) during 1900-2008. *Journal of Geophysical Research*, *116*, D12115. https://doi.org/10.1029/2010JD015541

van Dam, T., Wahr, J., Milly, P. C. D., Shmakin, A. B., Blewitt, G., Lavallée, D., & Larson, K. M. (2001). Crustal displacements due to continental water loading. *Geophysical Research Letters*, *28*, 651–654. https://doi.org/10.1029/2000GL012120

Dixon, T. H., Norabuena, E., & Hoteling, L. (2003). Paleoseismology and Global Positioning System: Earthquake-cycle effects and geodetic versus geologic fault slip rates in the Eastern California shear zone. *Geology*, *31*(1), 55–58. https://doi.org/10.1130/0091-7613(2003)031<0055:PAGPSE>2.0.CO;2

Famiglietti, J. S., Lo, M., Ho, S. L., Bethune, J., Anderson, K. J., Syed, T. H., et al. (2011). Satellites measure recent rates of groundwater depletion in California's Central Valley. *Geophysical Research Letters*, *38*, L03403. https://doi.org/10.1029/2010GL046442

Faunt, C. C., Sneed, M., Traum, J., & Brandt, J. T. (2016). Water availability and land subsidence in the Central Valley, California, USA. *Hydrogeology Journal*, *24*(3), 675–684. https://doi.org/10.1007/s10040-105-1339-x.

Fay, N. P., Bennett, R. A., & Hreinsdóttir, S. (2008). Contemporary vertical velocity of the central Basin and Range and uplift of the southern Sierra Nevada. *Geophysical Research Letters*, *35*, L20309. https://doi.org/10.1029/2008GL034949

Feng, L., & Newman, A. V. (2009). Constraints on continued episodic inflation at Long Valley Caldera, based on seismic and geodetic observations. *Journal of Geophysical Research*, *114*, B06403. https://doi.org/10.1029/2008JB006240

Fialko, Y., Simons, M., & Khazan, Y. (2001). Finite source modeling of magmatic unrest in Socorro, New Mexico, and Long Valley, California. *Geophysical Journal International*, *146*(1), 191–200. https://doi.org/10.1046/j.1365-246X.2001.00453.x

Fu, Y., Freymueller, J. T., & Jensen, T. (2012). Seasonal hydrological loading in southern Alaska observed by GPS and GRACE. *Geophysical Research Letters*, *39*, L15310. https://doi.org/10.1029/2012GL052453

Gee, M. A., Taylor, R. N., Thirlwall, M. F., & Murto, B. J., (1998). Glacioisotacy controls chemical and isotopic characteristics of tholeiites form the Reykjanes Peninsula, SW Iceland, *Earth and Planetary Science Letters*, *164*, 1–5, 1-2, DOI: https://doi.org/10.1016/S0012-821X(98)00246-5.

Grapenthin, R., Sigmundsson, F., Geirsson, H., Arnadóttir, T., & Pinel, V. (2006). Icelandic rhythmics: Annual modulation of land elevation and plate spreading by snow load. *Geophysical Research Letters*, *33*, L24305. https://doi.org/10.1029/2006GL028081

Hammond, W. C., Blewitt, G., & Kreemer, C. (2016). GPS Imaging of vertical land motion in California and Nevada: Implications for Sierra Nevada uplift. *Journal of Geophysical Research: Solid Earth*, *121*, 7681–7703. https://doi.org/10.1002/2016JB013458

Hammond, W. C., Blewitt, G., Li, Z., Kreemer, C., & Plag, H.-P. (2012). Contemporary uplift of the Sierra Nevada, western United States, from GPS and InSAR measurements. *Geology*, *40*(7), 667–670. https://doi.org/10.1130/G32968.1

Hammond, W. C., & Thatcher, W. (2007). Crustal deformation across the Sierra Nevada, Northern Walker Lane, Basin and Range transition, western United States measured with GPS, 2000-2004. *Journal of Geophysical Research*, *112*, B05411. https://doi.org/10.1029/2006JB004625

Hatch, R., Ruhl, C., Smith, K., & Abercrombie, R. (2017). Moderate sized events (3 M_w 5.4-5.6) and aftershock relocations of the 2016-2017 Nine Mile Ranch earthquake sequence near Hawthorne, Nevada. *Seismological Research Letters*, *88*(2B), 463–723. https://doi.org/10.1785/0220170035

Heki, K. (2000). Seasonal modulation of interseismic strain buildup in Northeastern Japan driven by snow loads. *Science*, *293*(5527), 89–92. https://doi.org/10.1126/science.1061056

Hetland, E. A., Musé, P., Simons, M., Lin, Y. N., Agram, P. S., & DiCaprio, C. J. (2012). Multiscale InSAR Time Series (MInTS) analysis of surface deformation. *Journal of Geophysical Research*, *117*, B02404. https://doi.org/10.1029/2011JB008731

Hill, D. P. (2006). Unrest in Long Valley Caldera, California, 1978–2004. In C. Troise, G. de Natale, & C. R. J. Kilburn (Eds.), *Mechanisms of Activity and Unrest at Large Calderas*, *Geological Society, London, Special Publications*, (Vol. 269, pp. 1–24).

Jellinek, A. M., Manga, M., & Saar, M. O. (2004). Did melting glaciers cause volcanic eruptions in eastern California? Probing the mechanics of dike formation. *Journal of Geophysical Research*, *109*, B09206. https://doi.org/10.1029/2004JB002978

Ji, K. H., Herring, T. A., & Llenos, A. L. (2013). Near real-time monitoring of volcanic surface deformation from GPS measurements at Long Valley Caldera, California. *Geophysical Research Letters*, *40*, 1054–1058. https://doi.org/10.1002/grl.50258

Johnson, C. W., Fu, Y., & Bürgmann, R. (2017). Seasonal water storage, stress modulation, and California seismicity. *Science*, *356*(6343), 1161–1164. https://doi.org/10.1126/science.aak9547

Jull, M., & McKenzie, D. (1996). The effect of deglaciation on mantle melting beneath Iceland. *Journal of Geophysical Research*, *101*, 21,815–21,828.

Kreemer, C., Hammond, W.C., Blewitt, G., Holland, A. A., & Bennett, R. A. (2012). A geodetic strain rate model for the Pacific-North American plate boundary, western United States. scale 1:1,500,000, Nevada Bureau of Mines and Geology publication M178.

Kreemer, C., & Zaliapin, I. (2018). Spatio-temporal correlation between seasonal variations in seismicity and horizontal dilatational strain in California. *Geophysical Research Letters*, *45*, 9559–9568. https://doi.org/10.1029/2018GL079536

Langbein, J. (2003). Deformation of the Long Valley Caldera, California: Inferences from measurements from 1988 to 2001. *Journal of Volcanology and Geothermal Research*, *127*(3-4), 247–267. https://doi.org/10.1016/S03777-0273(03)00172-0.

Langbein, J., Dzurisin, D., Marshall, G., Stein, R., & Rundle, J. (1995). Shallow and peripheral volcanic sources of inflation revealed by modeling two-color geodimeter and leveling data from Long Valley caldera, California, 1988-1992. *Journal of Geophysical Research*, *100*(B7), 12,487–12,495. https://doi.org/10.1029/95JB01052

Langbein, J., Hill, D., Parker, T. N., & Wilkinson, S. K. (1993). An episode of reinflation of the Long Valley Caldera, eastern California: 1989–1991. *Journal of Geophysical Research*, *98*(B9), 15,851–15,870. https://doi.org/10.1029/93JB00558

Lee, J., Rubin, C. M., & Calvert, A. (2001). Quaternary faulting history along the Deep Springs fault, California. *GSA Bulletin*, *113*(>7), 855–869.

Lifton, Z., Newman, A. V., Frankel, K. L., Johnson, C. W., & Dixon, T. H. (2013). Insights into distributed plate rates across the Walker Lane from GPS geodesy. *Geophysical Research Letters*, *40*, 4620–4624. https://doi.org/10.1002/grl.50804

Lisowski, M. (2007). Analytical volcano deformation source models. In *Volcano Deformation, Springer Praxis Books* (Chap. 8, pp. 279–304). Berlin, Heidelberg: Springer. https://doi.org/10.1007/978-3-540-49302-0_8

Lowenstern, J. B., Sisson, T. W., & Hurwitz, S. (2017). Probing magma reservoirs to improve volcano forecasts. *Eos*, *98*. https://doi.org/10.1029/2017EO085189

Luthcke, S. B., Sabaka, T. J., Loomis, B. D., Arendt, A. A., McCarthy, J. J., & Camp, J. (2013). Antarctica, Greenland and Gulf of Alaska land ice evolution from an iterated GRACE global mascon solution. *Journal of Glaciology*, *59*(216), 613–631. https://doi.org/10.3189/2013JoG12J147

Maclennan, J., Jull, M., McKenzie, D., Slater, L., & Grönvold, K. (2002). The link between volcanism and deglaciation in Iceland. *Geochemistry, Geophysics, Geosystems*, *3*(11), 1062. https://doi.org/10.1029/2001GC000282

Marshall, G. A., Langbein, J., Stein, R. S., Lisowski, M., & Svarc, J. (1997). Inflation of Long Valley caldera, California, Basin and Range strain, and possible Mono Craters dike opening from 1990–94 GPS surveys. *Geophysical Research Letters*, *24*(9), 1003–1006. https://doi.org/10.1029/97GL00885

McCaffrey, R. (2005). Block kinematics of the Pacific–North America plate boundary in the southwestern United States from inversion of GPS, seismological, and geologic data. *Journal of Geophysical Research*, *110*, B07401. https://doi.org/10.1029/2004JB003307

Mogi, K. (1958). Relations between the eruption of various volcanoes and the deformation of the ground surface around them. *Bulletin of the Earthquake Research Institute-University of Tokyo*, *36*, 99–134.

Montgomery-Brown, E. K., Wicks, C. W., Cervelli, P. F., Langbein, J. O., Svarc, J. L., Shelly, D. R., et al. (2015). Renewed inflation of Long Valley Caldera, California (2011 to 2014). *Geophysical Research Letters*, *42*, 5250–5257. https://doi.org/10.1002/2015GL064338

Newman, A., Dixon, T., & Gourmelen, N. (2006). A four-dimensional viscoelastic deformation model for Long Valley Caldera, California, between 1995 and 2000. *Journal of Volcanology and Geothermal Research*, *150*(1-3), 244–269. https://doi.org/10.1016/j.jvolgeores.2005.07.017

Oldow, J. S., Aiken, C. L. V., Hare, J. L., Ferguson, J. F., & Hardyman, R. F. (2001). Active displacement transfer and differential block motion within the central Walker Lane, western Great Basin. *Geology*, *29*(1), 19–22. https://doi.org/10.1130/0091-7613(2001)029<0019:ADTADB>2.0.CO;2

Palmer, W. C. (1965). *Meteorological Drought*, *Res. Paper* (Vol. 45, p. 58). Washington, DC: Dept. of Commerce.

Petersen, M. D., Zeng, Y., Haller, K. M., McCaffrey, R., Hammond, W. C., Bird, P.,et al. (2014). Geodesy- and geology-based slip-rate models for the Western United States (excluding California) national seismic hazard maps. *U.S. Geological Survey Open-File Report 2013–1293*, 63 80 p. https://doi.org/10.3133/ofr20131293

Savage, J. C. (1988). Principal component analysis of geodetically measured deformation in Long ValleyCaldera, Eastern California, 1983–1987. *Journal of Geophysical Research*, *93*(B11),13,297–13,305. Savage, J. C., & Clark, M. M. (1982). Magma resurgence in Long Valley Caldera, California: Possible cause of the 1980 Mammoth Lakes earthquakes. *Science*, *217*(4559), 531–533. https://doi.org/10.1126/science.217.4559.531

Savage, J. C., Gan, W., & Svarc, J. L. (2001). Strain accumulation and rotation in the Eastern California Shear Zone. *Journal of Geophysical Research*, *106*(B10), 21,995–22,007.

Shen, Z.-K., Jackson, D. D., & Ge, B. X. (1996). Crustal deformation across and beyond the Los Angeles basin from geodetic measurements. *Journal of Geophysical Research*, *101*(B12), 27,957–27,980. https://doi.org/10.1029/96JB02544

Sigmundsson, F., Einarsson, P., Rögnvaldsson, S. T., Foulger, G. R., Hodgkinson, K. M., & Thorbergsson, G. (1997). The 1994-1995 seismicity and deformation at the Hengill triple junction, Iceland: Triggering of earthquakes by minor magma injection in a zone of horizontal shear stress. *Journal of Geophysical Research*, *102*(B7), 15,151–15,161. https://doi.org/10.1029/97JB00892

Sigmundsson, F., Pinel, V., Lund, B., Albino, F., Pagli, C., Geirsson, H., & Sturkel, E. (2017). Climate effects on volcanism: Influence on magmatic systems of loading and unloading from ice mass variations, with examples from Iceland. *Philosophical Transactions of the Royal Society A: Mathematical, Physical and Engineering Sciences*, *368*(1919), 2519–2534. https://doi.org/10.1098/rsta.2010.0042

Sigvaldason, G. E., Annertz, K., & Nilsson, M. (1992). Effect of glacier loading/deloading on volcanism: Postglacial volcanic production rate of the Dyngjufjöll area, central Iceland. *Bulletin of Volcanology*, *54*(5), 385–392. https://doi.org/10.1007/BF00312320

Thatcher, W., Foulger, G. R., Julian, B. R., Svarc, J., Quilty, E., & Bawden, G. W. (1999). Present-day deformation across the Basin and Range Province, Western United States. *Science*, *283*, 1714–1718.

Tiampo, K. F., Rundle, J. B., Fernandez, J., & Langbein, J. (2000). Spherical and ellipsoidal volcanic sources at Long Valley caldera, California, using a genetic algorithm inversion technique. *Journal of Volcanology and Geothermal Research*, *102*(3-4), 189–206. https://doi.org/10.1016/S0377-0273(00)00185-2

Wdowinski, S., Bock, Y., Zhang, J., Fang, P., & Genrich, J. (1997). Southern California permanent GPS geodetic array: Spatial filtering of daily positions for estimating coseismic and postseismic displacements induced by the 1992 Landers earthquake. *Journal of Geophysical Research*, *102*(B8), 18,057–18,070. https://doi.org/10.1029/97JB01378

Wesnousky, S. G. (2005). Active faulting in the Walker Lane. *Tectonics*, *24*, TC3009. https://doi.org/10.1029/2004TC001645

Wesnousky, S. G., Bormann, J. M., Kreemer, C., Hammond, W. C., & Brune, J. N. (2012). Neotectonics, geodesy, and seismic hazard in the Northern Walker Lane of Western North America: Thirty kilometers of crustal shear and no strike-slip? *Earth and Planetary Science Letters*, *329-330*, 133–140. https://doi.org/10.1016/j.epsl.2012.02.018

Wessel, P., Smith, W. H. F., Scharroo, R., Luis, J. F., & Wobbe, F. (2013). Generic Mapping Tools: Improved version released. *Eos, Transactions American Geophysical Union*, *94*(45), 409–410. https://doi.org/10.1002/2013EO450001

Zaliapin, I., & Ben-Zion, Y. (2013). Earthquake clusters in southern California. I: Identification and stability. *Journal of Geophysical Research: Solid Earth*, *118*, 2847–2864. https://doi.org/10.1002/jgrb.50179

Zeng, Y., & Shen, Z.-K. (2014). Fault network modeling of crustal deformation in California constrained using GPS and geologic observations. *Tectonophysics*, *612–613*, 1–17. https://doi.org/10.1016/j.tecto.2013.11.030

Zumberge, J. F., Heflin, M. B., Jefferson, D. C., Watkins, M. M., & Webb, F. H. (1997). Precise point positioning for the efficient and robust analysis of GPS data from large networks. *Journal of Geophysical Research*, *102*(B3), 5005–5017. https://doi.org/10.1029/96JB03860

References From the Supporting Information

Shelly, D. R., Ellsworth, W. L., & Hill, D. P. (2016). Fluid-faulting evolution in high definition: Connecting fault structure and frequency-magnitude variations during the 2014 Long Valley Caldera, California, earthquake swarm. *Journal of Geophysical Research: Solid Earth*, *121*, 1776–1795. https://doi.org/10.1002/2015JB012719